Single-Photon Detector Calibration

Sergey V. Polyakov
National Institute of Standards and Technology, Gaithersburg, MD 20899
(Dated: July 7, 2015)

I. INTRODUCTION

As we have seen thus far, single-photon detectors are based on a variety of non-trivial physical phenomena and often employ complex circuitry. Therefore, thorough characterization of a detector's properties is necessary before they can be relied on for accurate measurements. To this end, it is important to establish a uniform way to characterize photon detectors as accurately as possible regardless of the differences in their underlying technology. Such an undertaking reveals the interconnectedness of detector's properties. As an example, detection efficiency is often considered the most critical parameter of a detector. However, it is by far not the only relevant parameter, and its usefulness is greatly reduced when presented without considerable additional information. Due to the inherent nonlinearity (saturation) of many single-photon detectors, the apparent detection efficiency depends critically on the count rate and photon statistics for which the efficiency is measured (or defined). Even when one attempts to more stringently qualify detection efficiency and its definition, the complex response of single-photon detectors makes it impossible to extrapolate to the wide range of input conditions to which the device may be subjected. Characterization of detectors, therefore, requires much more than a simple measurement of the detection efficiency. A set of additional parameters, such as the dead and reset times (c.f. Chapter 2) and the afterpulsing characteristics, are needed to describe a typical non-photon-number resolving detector. Photon-number resolving (PNR) detectors (with a notable exception of detectors with full PNR capability, such as transition edge sensors (TES)) often call for an even more thorough characterization: a measurement of its positive-operator-valued measure (POVM). (see Chapter 2 for definition of PNR capability)

Unless a detector's response is truly linear with respect to an input photon number (i.e. unless a detector is a true PNR detector), the statistical properties of input light fields further complicate the measurement situation. Because input sources may have different auto-correlations (poissonian, bunched (thermal), or antibunched), and because, in general, a single-photon detector's efficiency is time-dependent, different fractions of the incoming photons will be detected, missed, or counted more than once. In addition, detectors can produce counts in the absence of an input photon field, resulting in dark counts whose statistical properties are not related to those of the input field. There can also be a background field whose photon statistics are uncorrelated with the input light. Thus care should be taken to understand the impact of statistical properties of the actual input field on the detector parameters measured during characterization and calibration.

Given all these complications, a model of a detector's response should be developed and verified before any characterization takes place. To prove that the model for a detector is consistent an independent verification of the calibration results obtained for a particular type of detector is necessary.

In this chapter we introduce the set of detector properties, common to most contemporary detectors, that should be determined for a complete characterization. Then we introduce methods for detector characterization, and finally we present practical recipes for calibration of non-PNR detectors and PNR detectors with full PNR capability. Although the recipes are based on specific underlying technologies (we use as examples single-photon avalanche diodes (SPADs) and TES detectors), the measurement algorithms are in general applicable to detectors with other principles of operation. A radically different approach is treating a detector as a black box, i.e. to pay no attention to the underlying principles of operation and approach the problem from the viewpoint of quantum measurement theory to characterize the detection of arbitrary input quantum states (i.e. find a detector's POVM), although in practice, even with such an approach some assumptions about the detector's operation are necessary to make the measurement problem tractable. Such a characterization is particularly useful for PNR detectors with saturation. POVM measurements are addressed in chapter 9.

II. DEFINITIONS

Key properties of detectors based on a range of underlying principles have been introduced in the preceding chapters. Here we establish a generalized list of parameters that are relevant to calibrations with accuracies down to the $\approx 0.1\%$ level. More accurate calibrations may require considering additional parameters.

A. Recovery time, dead time and reset time

Many detectors, such as SPADs and single SNSPDs, can generally detect only one photon of the input field at a time, after which they become insensitive to incoming radiation for a certain amount of time. This period of time is called the device's dead time. Note also that returning to operation from this insensitive (dead) state may be a complex process, during which both the ability to detect photons and the device's detection latency (i.e. the time between a photon entering the detector and a signal output, see Chapter 2) can differ significantly from that of normal operation. This mode of a detector is called reset time. The above two modes of a detector, when the detector's operation is abnormal, are called the recovery time. Although the instantaneous detection efficiency at any point during this transient period may be a function of time elapsed since the detection event, one possible simplification useful for characterization with cw sources is assuming a constant detection efficiency when the detector is alive and zero detection efficiency when the detector is dead, and adjusting an effective dead time accordingly. A calibration method should be adapted to properly handle parameter fluctuations.

B. Detection Efficiency

Detection efficiency is commonly thought as the probability of a detector to produce a successful detection given a single-photon input, when the detector is operating normally (far from its previous recovery), η_{DE}. Because of the dead time, (and assuming that both afterpulsing and dark count rates are zero), the actual rate of detection R_{out} will be bound by $R_{out} \leq \eta_{\mathrm{DE}} R_{\mathrm{in}}$, where R_{in} is the rate of incoming photons. Obviously, knowing just η_{DE} is not enough to describe the operation of a detector with realistic input fields. Alternatively, detection efficiency can be defined as a proportionality coefficient η_{cond} relating the number of detection signals to the number of photons that impinged on a detector, the auto-correlation properties of the input field, etc.

The detection efficiency of a full PNR detector is defined in a similar fashion. This probability should scale with the number of incident photons. That is, if η_{DE} is the probability to detect a single photon given a single-photon input, the η_{DE}^2 is the probability to detect a photon pair given two input photons, and in general η_{DE}^n is the probability to detect n photons given an n-photon state input. Any deviation of a real-life device from a full PNR assumption can significantly limit accuracy of a precision measurement.

C. Dark counts

Dark counts are output signals produced by a detector that do not correspond to actual photon detections. In most cases, nothing about the processes that cause dark counts makes them distinguishable from photon detection events. It is often assumed that dark counts obey Poissonian statistics (although at very high count rates that may no longer be true because of dead time effects). For an accurate calibration, dark count rates need to be characterized and included in the analysis.

D. Afterpulsing

Afterpulsing counts occur some time after a detection, sometimes even during the recovery of the detector to its normal mode. These counts originate from within the detector, and not from incoming photons. Particularly, in semiconductor avalanche detectors (see Chapter 4) afterpulses are triggered by carriers that were trapped and subsequently released from localized trap sites in the avalanche region after a previous avalanche. In a calibration the afterpulsing probability needs to be characterized as well.

III. CALIBRATION METHODS

In metrology, *primary standard methods* stand out because they depend on parameters of the physical system that can be independently verified by measurement and they do not depend on implementation. In radiometry, a blackbody is a good electromagnetic source standard because there is a direct and universal dependence between electromagnetic radiation and temperature, as established by Planck [1]. A synchrotron is another such source, because its radiation is only related to velocity, charge and number of particles, and the magnetic field strength. That is, because the properties of the electromagnetic radiation can be fully described by just these few parameters, one can reproduce

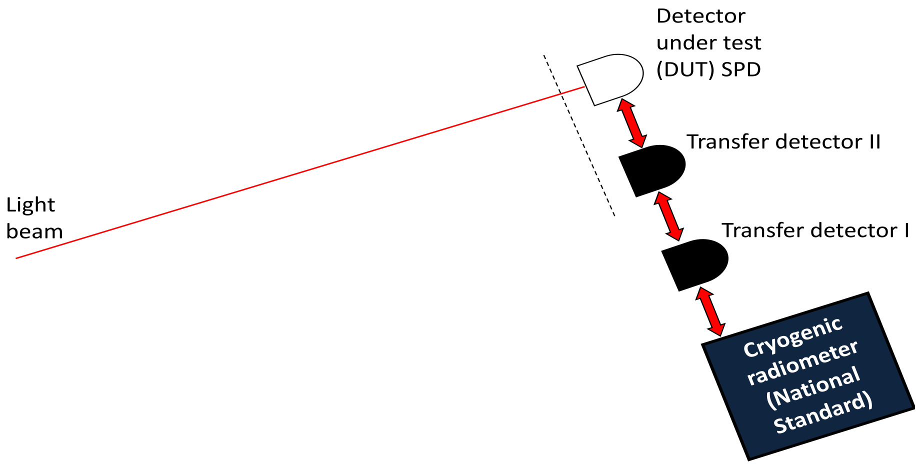

FIG. 1: Conventional detection efficiency calibration based on radiant power measurements (detector substitution). SPD - single-photon detector.

these sources and independently measure (or calibrate) the response of their radiometric equipment. This procedure independently reproduces a measurement scale for radiant power. Both synchrotron and blackbody are examples of a so-called fundamentally absolute calibration techniques or "primary standard methods."

It turns out that with photon-counting detectors an additional primary standard method applies. This special method is based on quantum sources that produce photons in pairs, so that a detection of one photon of the pair indicates the presence of another - a so-called correlated-photon-pair calibration method.

As we established, practical calibration techniques may need to be adapted to the specifics of the photon counting devices under consideration. In this regard, because the photon-pair-based method is inherently based on direct photon counting, adapting this method to a photon-counting detector may be more straighforward than adapting a precision radiant-power-measurement-based method. In addition, the photon-pair-based calibration method may help with a more complete detector characterization, as will be seen later in the chapter.

We now outline the calibration methods as they apply to idealized detectors. By ideal, we mean that there are no competing mechanisms causing detectors to fire other than input signal used for calibration. Then, we will introduce operational models of non-ideal detectors and study their consequences.

A. Radiant power measurements (Substitution Method)

Optical detectors are calibrated by measuring the radiant power emitted by a calibrated source. That source may be a primary standard, or a transfer standard (a detector whose calibration is tied ultimately to either a primary standard source or primary standard detector). Primary standard sources are typically one of two types: blackbodies or synchrotrons. A blackbody source is used as a primary standard for visible and near-infrared spectral bands. Synchrotron radiation can be used as a primary standard source over a broad spectral range, particularly in the ultra-violet band. Currently all transfer detectors are classical detectors, whose output is proportional to radiant power. Using one or more transfer detectors (or directly using a primary standard detector if one has access to such a device) is referred to as the substitution method, see Fig. 1, because the transfer detector is swapped with a detector under test (DUT) during calibration. Often, employing a transfer detector is advantageous to using a primary standard detector, despite the added systematic uncertainties, because the established procedures for calibrating transfer standards (classical detectors) are mature and well-characterized. From the standpoint of a photon-counting detector, the issues of power measurements are often more problematic regardless of the input source of optical radiation. The main difficulty is converting radiant power into photon flux. And even if detectors were perfect, an additional accurate measurement of the source's spectrum is also needed. Other issues with single-photon detectors further complicate a power measurement. These issues will be discussed later in our case study of a substitution calibration.

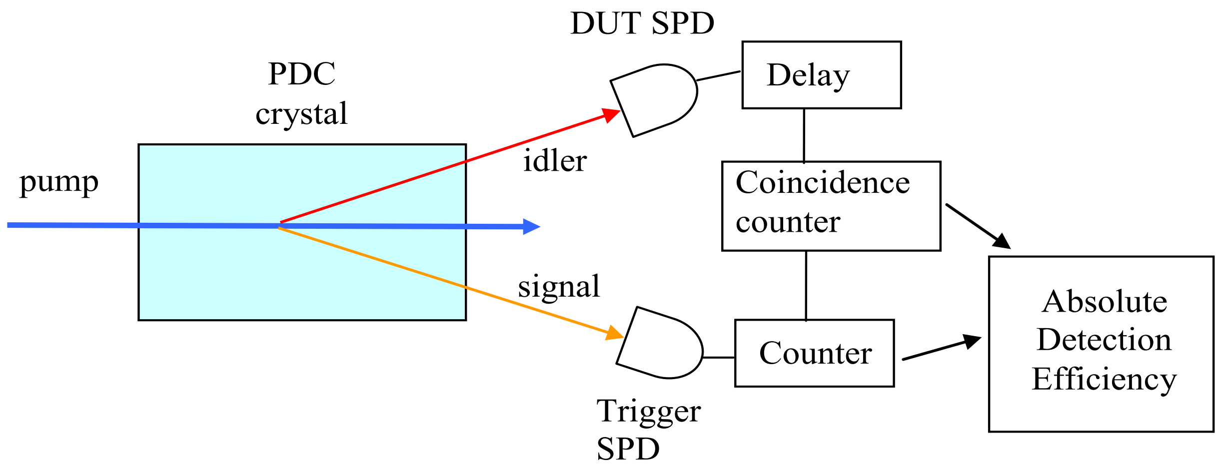

FIG. 2: Detection-efficiency measurement based on photon-pair generation via parametric down-conversion.

B. Correlated-Photon-Pair Calibration Method

The photon pairs produced in spontaneous parametric down-conversion (PDC), c.f. Chapter 12, provide a fundamentally absolute way to calibrate single-photon detectors [2–19]. In PDC, photons are produced in pairs whose frequencies and wavevectors are governed by energy and momentum conservation. Therefore the detection of one photon provides spatial, spectral, and temporal location information about (or *heralds*) the other photon of the pair with certainty. The absolute nature of the method derives from this quantum property of a PDC light source. Therefore, this method is a primary standard method. [20] Because the method relies on individual photon detections as a trigger, the scheme operates directly in the photon-counting regime and is thus well suited for photon-counting devices. To measure detection efficiency, a trigger detection system is placed to intercept some of the down-converted light. A DUT is then arranged to collect all the photons correlated to those seen by the trigger detector. The DUT channel detection efficiency is the ratio of the number of coincidence events to the number of trigger detection events in a given time interval. Coincidences are usually measured with start-stop time to digital systems, with the heralding detector output connected to the start, and the DUT output to the stop, Fig. 2. If we specify the total efficiency of the DUT and trigger channels by $\eta_{\rm DUT}$ and $\eta_{\rm trig}$, respectively, then the total number of trigger counts is

$$N_{\rm trig} = \eta_{\rm trig} N_{\rm p} \tag{1}$$

and the total number of coincidence counts is

$$N_{\rm c} = \eta_{\rm DUT}\eta_{\rm trig} N_{\rm p}, \tag{2}$$

where $N_{\rm p}$ is the total number of down-converted photons emitted into the trigger channel during the counting period. The absolute detection efficiency of the DUT channel is then simply

$$\eta_{\rm DUT} = \frac{N_{\rm c}}{N_{\rm trig}}. \tag{3}$$

Note that this is the efficiency of the entire detection channel (including collection optics, etc.) and not just the efficiency of the DUT alone [21, 22]. Therefore, all losses in the DUT path before reaching a detector must be determined. This includes losses within the source, usually a nonlinear crystal. Another important possible source of loss is the overlap between heralded photons that are correlated with trigger photons and the field of view of a DUT channel. Total channel efficiency is the product of the transmittances of individual optical elements in a DUT path and any beam matching efficiencies, like the collection mode overlap. Uncertainties in characterizing these losses contribute to the overall uncertainty budget. Other uncertainties may also be present, but they are detector-specific.

With ideal detectors, the correlation function between the firing of the herald detector and the DUT would appear as shown in Fig. 3 (a). Here, the tallest correlation peak corresponds to the correlated signal due to PDC. It sits on a background that is generated by accidental or uncorrelated events, due to finite detection efficiency in both channels. Before applying formula (3), this background should be removed. Then, the remaining number of correlated events gives $N_{\rm c}$.

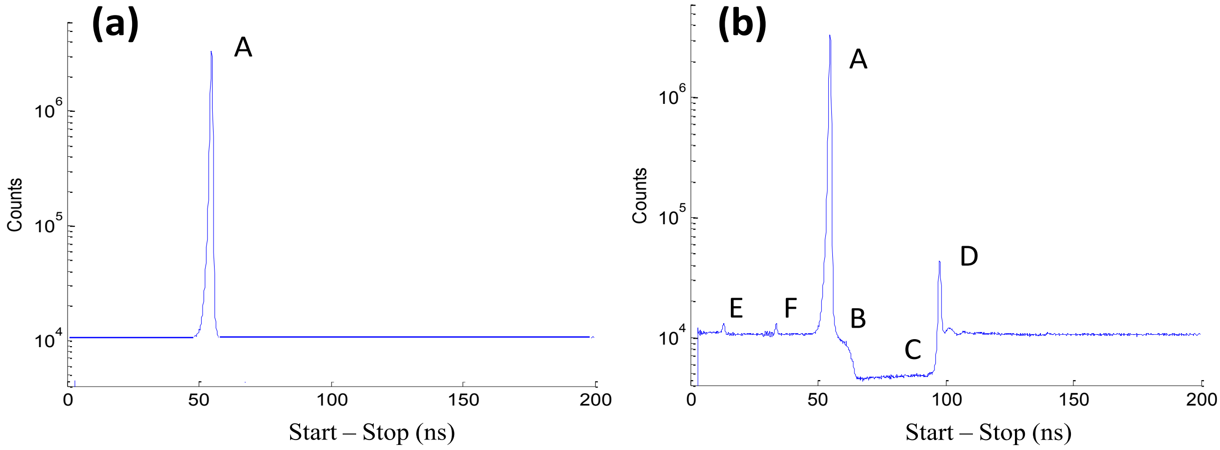

FIG. 3: Start-Stop histograms that correspond to a correlated-pair calibration method with idealized detectors (a) and real detectors (b). In both cases the background is due to finite detection efficiency of a heralding detector (with real detectors, dark counts will also contribute to a background, but such contribution is small in this example). Features are identified as follows: A – main correlation peak, B – correlated photons that have arrived simultaneously with those in peak A, during the reset mode of a detector, exhibiting longer latency times. C – reduction of stop counts due to recovery time of a detector. D – peak due to afterpulses and delayed counts in the reset mode (twilight counts). E, F – peaks specific to the setup, and not the DUT.

IV. PRACTICAL CONSIDERATIONS

The basic theory discussed above assumes an ideal single-photon detector. Namely, the DUT produces a count with constant probability (for a single-photon input) that depends only on the detector efficiency and does not depend on any other factors; the detector should never produce a count if no photons were present; the single-photon detector is assumed to have no recovery time, etc. Below we discuss practical approaches to calibrating a real-world non-photon-number resolving detector (a SPAD) and a photon-number resolving detector (a TES).

A. Semiconductor Single-Photon Avalanche Diodes

1. Model of a single-photon detector

Real-world detectors suffer from multiple features that complicate their output. To achieve high accuracy, all the features of single-photon detectors must be characterized first. Many of these features leave a trace on the correlation function as shown in Fig. 3 (b). Such histograms can be readily used to build a model of a real-world detector. Here we demonstrate how to build a model of a typical click/no-click single-photon detector based on such a correlation measurement, using a silicon SPAD as an example [23]. The recipe presented here can be modified to characterize any non-PNR detector. Building a detector model is important for both correlated measurements and radiant power measurements. On one hand, to find N_c for correlated measurements it is necessary to separate the correlated signal, due to true detections of twin photons, from background photons, with a high degree of accuracy. Measurements of radiant power on the other hand should be corrected for dark counts and afterpulsing, events that are not due to a photon detection.

We start with a correlated measurement, and obtain a histogram. We first note all features (peaks, valleys, etc.) of the histogram (see Fig. 3 (b)) and determine their origins. In this example, features are labeled with letters A through F. The main coincidence peak (A) is the most prominent feature of the histogram and represent correlated events.

The trench (labeled C) to the right of the peak is due to detector dead time. Because the DUT often fires due to detection of a photon from a correlated pair (feature A), it enters its recovery time, during which it is unable to fire again (due to background photons). Thus, the number of background events shortly after A is reduced. When subtracting a background, this trench needs to be properly modeled (to be correctly removed).

The origin of the small "shoulder" (labeled B) on the right the main coincidence peak is less obvious. A study of this feature shows that the "shoulder" events are valid photon detections for which the detector latency is unusually

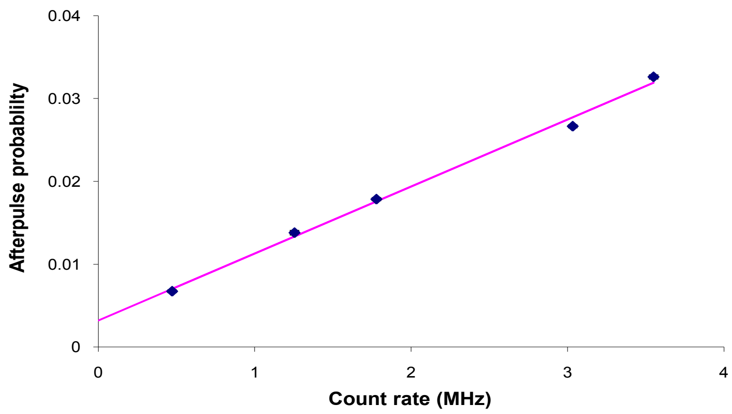

FIG. 4: Afterpulsing probability of the DUT at various count rates. The apparent increase in afterpulsing probability with count rate is due to the twilight sensitivity of the detector, as photons arriving during the reset time (c.f. Chapter 2) trigger an avalanche with increased latency. The probability of true afterpulsing (due to trapped carriers) remains constant, and can be found by extrapolation of the linear dependence to low count rates.

long. This happens when a photon arrives while the detector is in the midst of its reset from a prior detection (c.f. Chapter 2). In this case, the detector may still manage to output an electric signal, but with an unusually long latency. Due to the inherent uncertainty associated with characterization of this additional complexity, this effect should be avoided when possible by reducing the photon flux. (In the comparison experiment discussed here, high photon rates are unavoidable, because of the use of classical transfer standard detectors.) Because this behavior occurs during the device's return from its dead state, we refer to these detections as "twilight" events.

The afterpulse feature (D) is also affected by this mechanism. That is, events that occur due to variations in detector sensitivity and latency during the reset time can pile up in the vicinity of the afterpulse peak, causing the perceived probability of an afterpulse to be count-rate dependent. However, the probability of a purely electronic afterpulse (that is, an afterpulse due to trapped charge that was released during the reset time) should not depend on count rate. The contribution from twilight events is due to real photons. We verify this by measuring the number of events in the afterpulse peak as a function of count rate, and observe that, indeed, the afterpulse probability is a linear function of count rate with a positive offset, Fig. 4. This feature is very important for radiant power measurements because only proper afterpulses should be accounted for when calculating the number of photons detected. Also, due to the same effect, the true dead time of a real detector (i.e. when it detection efficiency is zero) is shorter than what is suggested by the duration of the dip C.

To demonstrate the twilight effect, and measure its properties directly, one can send pairs of attenuated optical pulses separated by a controllable delay to a detector, and record the output with a coincidence board. Fig. 5 shows a number of histograms for varying delay times between the two optical pulses detected by a SPAD with a nominal recovery time of 49.5 ns. We see that if the photon comes during the first ≈ 40 ns of the recovery time, i.e. while the active quench circuit has the bias below breakdown (c.f. Chapter 4) it has no effect on the afterpulse (so the dead time is just ≈ 40 ns!). In such a case, the afterpulse has a shape shown by the thick black line in Fig. 5 (previously observed in Ref. [24]). If the two light pulses are separated by more than ≈ 40 ns, so the second pulse arrives while the SPAD bias is rising back to its original value, the counts in the afterpulse feature increase and we see a distinct new peak in the afterpulse shape, which can be delayed by up to 10 ns from the normal latency time. The data shows that the closer the photon arrives to the end of the recovery time, the shorter the observed delay (see the upper curve in Fig. 5), [23]. We conclude that the time after a detection when the SPAD does not put out any signal (c.f. feature C in Fig. 3 (b)) is not equal to the dead time (and does not have to be equal to recovery time). The electronic pulses that represent these counts are delayed by up to the duration of the reset time, contributing to a higher-than-normal afterpulse peak D in Fig. 3 (b). The same mechanism is behind feature B. It appears due to correlated counts, i.e. by photons that arrive at the same time as these of peak A. The only difference is that the detector is in its reset time, recovering from an earlier background detection. Note here that the extent of the reset time and latency profile of twilight counts depend strongly on the detector's underlying technology and its electronics.

Other, tiny peaks in Fig. 3 (b) (E and F) may also be present and are specific to our particular setup. Most notably, peak E is produced by afterpulsing of the trigger detector. This is a very important point, because ideally, correlated-photon calibration techniques should not depend on the properties of the trigger detector. In this case,

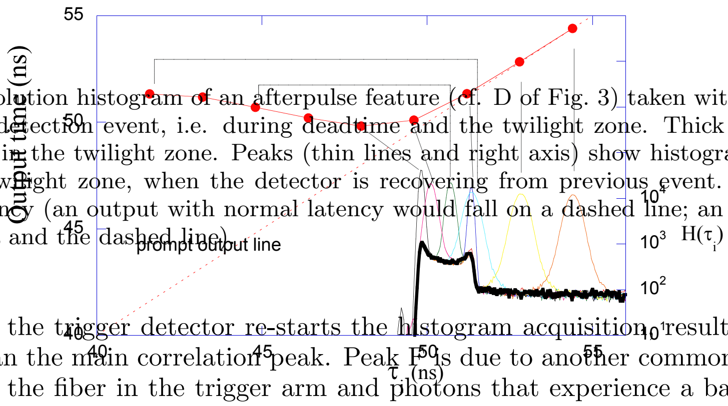

FIG. 5: High resolution histogram of an afterpulse feature (cf. D of Fig. 3) taken with photons arriving with a range of delays after a previous detection event, i.e. during deadtime and the twilight zone. Thick line shows an afterpulse feature with no photons arriving in the twilight zone. Peaks (thin lines and right axis) show histogram counts (in 4ps bins) due to a photon arriving in the twilight zone, when the detector is recovering from previous event. Upper curve (dots and left axis) shows variations in latency (an output with normal latency would fall on a dashed line; an extra delay is indicated by the difference between the data and the dashed line).

an afterpulse of the trigger detector re-starts the histogram acquisition, resulting in detecting correlated photons ≈ 55 ns earlier than the main correlation peak. Peak F is due to another common issue: there is a small back-reflection at either end of the fiber in the trigger arm and photons that experience a back-reflection at both ends of the fiber arrive at the trigger SPAD after traveling two extra fiber lengths. In the case of Fig. 3 the fiber is 2 m long and this extra double-pass corresponds to a delay of ≈ 20 ns. Again, the coincidences in this peak are valid and should be included in our determination of the true number of coincidences.

As shown, the use of just the correlation histogram allows one to identify a broad range of effects, even those whose contribution is minute (features E and F contain less than 0.5% of relevant counts). One remaining concern is that a click/no-click detector is generally not able to discriminate the instantaneous arrival of more than one photon from the arrival of a single photon. This needs to be addressed in the calibration model, particularly for a pulsed photon source [25].

The above study gives rise to the following model of a photon-counting detector:

- A detector has a constant detection efficiency η_{DE} when it is counting, and 0 when it is dead. This is a simplification, because the detection efficiency is not really constant during the reset time.

- A detector has a recovery time, t_{recovery}, that is longer than its actual dead time t_{dead} due to the device activity during the reset. With our model, we do not need to accurately measure t_{recovery}, t_{dead}. To do that, many extra measurements (leading to extra uncertainties) would be needed. Instead, to find the effective t_{reset} we make use of the integrated number of twilight counts, readily found from the slope of Fig. 4 and assuming a constant detection efficiency η_{DE} during the entire reset time. This simplification does not affect accuracy of the calibration. The effective t_{recovery} can be estimated from the histogram as the distance between the peak of features A and D in Fig. 3 (b). The effective dead time is then simply ($t_{\mathrm{recovery}} - t_{\mathrm{reset}}$). Note that this simplification allows us to skip integrating the actual variable detection efficiency over the nominal duration of the reset time.

- A true afterpulse is an event that is not due to a photon detection (i.e purely due to charge trapping in SPADs). Its probability is also found from Fig. 4.

2. Correlated calibration technique

The model introduced above helps separate the background and correlated signals seen in Fig. 3, which is key to an accurate characterization. For simplicity, we require that the background and dark count rates on the trigger detector are negligible. We begin with a measured histogram denoted by $H(\tau_i)$, where τ_i is the time delay from the start event for the i^{th} bin. Our goal is to separate the events represented by $H(\tau_i)$ into two categories: events correlated to the trigger pulse $C(\tau_i)$, such that $N_{\rm c} = \sum C(\tau_j)$, and background events $B_{\rm m}(\tau_i)$:

$$H(\tau_i) = C(\tau_i) + B(\tau_i). \tag{4}$$

Note that when we measure $\eta_{\rm DE}$, we would have to not only find C, but also estimate how many correlated events were *missed* since the detector may have been dead when the correlated photon arrived. Similarly, the detector might be dead when a background event would otherwise have been recorded due to either a previous background event or a previous correlated event.

Following our model of the detector, we can express the recovery time $t_{\rm recovery}$ in terms of the number of time bins $d = t_{\rm recovery}/(\tau_{i+1} - \tau_i)$. Usually, d may be considered an integer. We also assume that the number of background events in a given bin is relatively constant before correlated events arrive, and we define B_0 as the average number of background events recorded per bin. Then, the probability b of an *alive* detector to register a background count is given by:

$$b = B_0/(N_{\rm trig} - dB_0). \tag{5}$$

For ease of discussion, we will assume that the delay of the DUT channel is long enough that all of the correlated signals appear after the $d^{\rm th}$ histogram bin. Then, the background in the presence of the correlated signal is:

$$\begin{gathered} B(\tau_i) = H(\tau_j) = B_0 \qquad (i < d); \\ B(\tau_i) = b \times (N_{\rm trig} - \sum_{j=i-d}^{i-1} H(\tau_j) - \Delta(\tau_i)) \qquad (i \geq d). \end{gathered} \tag{6}$$

Note that the number in parenthesis is the number of scans where it was possible to record a background event in the bin. The sum gives the number of times that the detector was in recovery in the $i^{\rm th}$ bin due to events in one of the previous d bins. The function $\Delta(\tau_i)$ accounts for the situations where a subsequent, closely spaced trigger pulse resets the histogram before it reaches the $i^{\rm th}$ bin, a feature of some start-stop boards. (Note the background level decrease for large j's that can be seen in Fig. 3 (b)).

We can use Eq. 6 together with Eq. 4 to determine C. Recall that $N_{\rm c} = \sum C(\tau_j)$, summing over the main correlation peak (feature A), its shoulder and (features B) and the small features E and F (Fig. 3 (b)). We find $\eta_{\rm cond}$ for the DUT, using Eq. 3, and accounting for losses in the DUT channel:

$$\eta_{\rm cond} = \frac{\sum C(\tau_j)}{N_{\rm trig}}. \tag{7}$$

The sum over the feature D gives the total number of afterpulses plus twilight counts. The probability of an afterpulse-like event is then simply the ratio of the two sums. Performing this measurement at different DUT count rates, and measuring this probability gives rise to Fig. 4. A linear regression helps separate the true afterpulse probability ($p_{\rm afterpulse}$) from the probability of twilight counts, $p_{\rm twilight}|_{\rm cond}$. The ratio $d' = p_{\rm twilight}|_{\rm cond}/b$ gives the effective $t_{\rm reset}$, measured in numbers of histogram bins.

To find the detection efficiency of the DUT $\eta_{\rm DE}$ from the data above, we calculate the corrected histogram $Z(\tau_i)$ that accounts for the occasional situation when DUT is dead because of a background detection during the arrival of a correlated photon as:

$$Z(\tau_i) = \frac{C(\tau_i)}{N_{\rm trig} - \sum\limits_{j=i-d}^{i-d'} B(\tau_j) - \Delta(\tau_i)} N_{\rm trig}. \tag{8}$$

Here we implicitly assume that the probability of the source to generate more than one correlated pair of photons is negligible. In a last step, we use Eq. (3), where now $N_{\rm c} = \sum Z(\tau_j)$. Note, that because we applied all the corrections to $N_{\rm c}$, we should use $\eta_{\rm DE}$ instead of η_{DUT} (because corrections are designed to eliminate dependance on any prior events and extract a detection efficiency of an 'always-active' detector). We see that the series of correlated measurements coupled with the detector's model introduced above provide a characterization of the detector. Particularly, we can extract detection efficiencies $\eta_{\rm DE}$ and $\eta_{\rm cond}$, and find $p_{\rm afterpulse}$ and $t_{\rm recovery}$ and an effective $t_{\rm dead}$. In addition, a measurement of dark counts is required, though this measurement is trivial for most detectors. (Note that there exist detectors whose dark count rates are count rate dependent, characterization of such detectors is beyond the scope of this algorithm.) We still need to prove, however, that this characterization is complete and adequate. This issue will be addressed by comparing a correlated-photon based calibration to one based on a radiant power measurement.

3. *Radiant power measurements with single-photon detectors*

To use a radiant power approach for calibration of single-photon detectors, one needs a method that turns a photon count into radiant power. This seems straightforward, as the energy per photon is given by $E = h\nu$, where ν is a weighted average frequency for a given source. However, proper corrections to the raw data are needed for an accurate conversion.

Consider a photon-counting measurement (during the time t) of a Poissonian input field by a single-photon detector described by the model introduced above. Such a source produces photons with a constant probability. Specifically, a Poissonian source's output does not depend on the history of previous emissions. On the other hand, a detector's response strongly depends on the history of previous photon detection. Therefore, the total number of counts N_{total} must be corrected so that the discrepancy introduced by the detector's behavior is removed. Corrections must include dark counts N_{dark}, effective dead time ($t_{\mathrm{recovery}} - t_{\mathrm{reset}}$), and real afterpulsing (whose probability is $p_{\mathrm{afterpulse}}$). We write:

$$P = \eta_{\mathrm{DE}} E \frac{N_{\mathrm{total}} - N_{\mathrm{dark}} - p_{\mathrm{afterpulse}} N_{\mathrm{total}}}{t - N_{\mathrm{total}}(t_{\mathrm{recovery}} - t_{\mathrm{reset}})}. \tag{9}$$

This expression shows that to accurately measure radiant power much more information about the detector than just η_{DE} is needed. Because in a radiant power measurement only the overall number of counts is recorded and no time information for each detector click is retained, a separate set of measurements aimed at characterizing the temporal response of the detector is necessary. For a stationary Poissonian input, however, it is possible to avoid some of this characterization if we are only interested in observing that stationary process, we simply use η_{cond}, which takes care of saturation effects:

$$P = \eta_{\mathrm{cond}} E (N_{\mathrm{total}} - N_{\mathrm{dark}} - p_{\mathrm{afterpulse}} N_{\mathrm{total}})/t. \tag{10}$$

Finally, if we neglect the effect of dark counts, we can further simplify this formula:

$$P \approx \widetilde{\eta}_{\mathrm{cond}} E N_{\mathrm{total}}/t. \tag{11}$$

Values of both η_{cond} and $\widetilde{\eta}_{\mathrm{cond}}$ strongly depend on the input conditions, i.e. input count rate and photon number statistics. Note that in the framework of the detector model η_{cond} in Eq. (10) is exactly the same as the detection efficiency that is given by analysis of the start-stop histogram, equation (7). This is a very useful observation if detector-substitution method results are to be directly compared to the correlated-photon results.

This measurement can be applied to direct measurements with a primary standard source or calibration against a classical transfer detector (using a detector substitution method). The above formulae can be used to obtain radiant power for Poissonian sources. Sources with other statistical properties may require slight modification.

4. *Experimental Implementation: Calibration and Verification*

As we have seen, calibrating single-photon detectors requires adopting a model of the detector and characterizing the detector within the model. Because the end result critically depends on these assumptions, a calibration should not only be performed with one method, but its results should be verified against another independent method. It is possible to combine the two absolute calibration techniques discussed: correlation- and substitution- based, in a single experimental setup, as shown in Fig. 6. Because the coincidence events used for the two-photon calibration and the single-photon count rate of the DUT used for the conventional calibration can be recorded simultaneously, the two types of calibrations can be effectively conducted simultaneously. To obtain additional data for the substitution method, the DUT is replaced with a calibrated detector. In one example of such a comparison a 351 nm Ar^+ laser pumps a $LiIO_3$ crystal. The pump power is monitored by a dedicated detector. Nearly degenerate downconverted photons at ≈702 nm were sent to the two single-photon detectors (here SPADs were used): trigger and DUT. The DUT detector is mounted behind an aperture to reduce PDC light not correlated to that seen by the trigger, and a lens to collect the correlated light onto the DUT active area with ≈0.2 mm diameter. The independently calibrated transfer-standard photodetector is a cooled high-shunt resistance Si PIN photodiode. A pinhole mounted close to the Si PIN photodiode's surface was used to restrict the wings of the illuminating beam. In that way, the apertures of a SPAD and a Si PIN photodiode are equal. In addition, narrow spectral filters are introduced in both trigger and DUT channels. The spectral band of the trigger-arm filter F_{T} is narrow enough to select only a small portion of the photons created by the downconversion process. The spectral bandwidth of F_{DUT} is significantly wider and completely encompasses the correlated band defined by F_{T}. The signals from the trigger and DUT single-photon detectors are

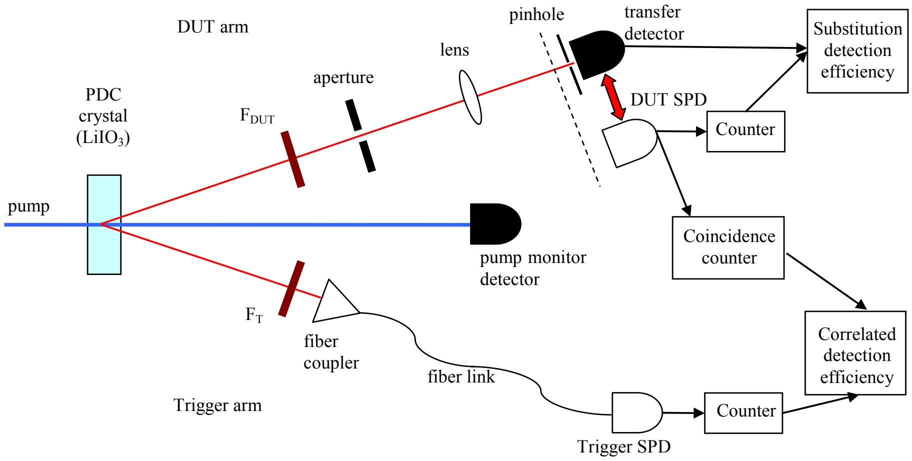

FIG. 6: Setup used for a calibration and verification experiment. This setup combines the two independent absolute calibration methods. SPD - single-photon detector. In the experiment described here SPADs were used.

Physical Property	Contribution to relative DE uncertainty (%)
Analog transfer standard calibration (QE equivalent)	0.10
Spatial nonuniformity of photodiode at 700nm, (standard deviation of central responsivity)	0.025
Analog measurement statistics and drift	0.06
Analog amplifier gain calibration at 10^{10} V/A	0.05
Pinhole backside reflection	0.1
DUT signal and background statistics	0.003
DUT afterpulsing	0.04
DUT dead time (due to rate changes with time)	0.02
Total	0.17

TABLE I: Uncertainty budget of a substitution calibration method.

collected by a circuit that records both the overall number of trigger and DUT events, and the correlation between trigger and DUT events in the form of a histogram with 0.1 ns temporal resolution. A typical histogram is shown in Fig. 3 (b).

Because the correlated method calibrates the entire optical path from within the nonlinear crystal to the DUT, as opposed to just the DUT detection efficiency, the transmittance of each optical element should be independently characterized. The uncertainties associated with those transmittance measurements will contribute to the overall uncertainty budget. An uncertainty budget with the list of physical properties typical for the radiant-power calibration method is presented in Table I, and the uncertainty budget for the correlated method is presented in Table II. The values for the uncertainties are taken from Ref. [19]. They are presented here to aid with estimating potential trade-offs, and identifying the properties that could potentially limit a final calibration. For example, it is evident that the uncertainty associated with photon statistics is not the limiting factor in these measurements. Because the number of single-photon detections can be increased to reach better accuracy, the accuracy of auxiliary measurements determines the limit. In particular, for the substitution calibration method, the major source of uncertainty is the calibration of the transfer detector, which accounts for 0.1% in the overall uncertainty figure. Traceable calibration of conventional detectors to a lower uncertainty is difficult [26]. For the correlation method, a major source of uncertainty is calibration of the filters F_{DUT}, F_{T}. To measure transmittance properties of the filters a dedicated SIRCUS [27] facility was used, whose accuracy is among the best worldwide.

One interesting property of parametric down-conversion is energy conservation. That is, the sum of energy of the pair of photons produced in the parametric interaction is equal to that of the single pump photon. Therefore, if the central frequency of the trigger channel frequency filter is ω_{T}, then the center frequency of conjugate pairs heralded by the trigger is $\omega_{\mathrm{DUT}} = \omega_{\mathrm{pump}} - \omega_{\mathrm{T}}$, where ω_{pump} is the frequency of pump. Thus, F_{T} filter in the trigger arm is conjugated with a certain range of frequencies in the DUT channel. This effect produces a so-called virtual

Physical Property	Contribution to relative DE uncertainty (%)
Crystal reflectance	0.02
Crystal transmittance	0.009
Lens transmittance	0.02
Geometric collection	0.04
DUT filter transmittance	0.09
Trigger bandpass to virtual bandpass wavelength	0.07
Histogram background subtraction	0.03
Coincidence circuit correction	0.08
Counting statistics	0.07
dead time (due to rate changes with time)	0.022
Trigger afterpulsing	0.06
Trigger background and statistics	0.01
Trigger signal due to uncorrelated photons	0.033
Trigger signal due to fiber back reflection	0.003
Total	0.18

TABLE II: Uncertainty budget of a correlated calibration method.

bandpass filter in the DUT channel, whose spectral shape and transmittance can be found from the spectral shape and transmittance of F_{T} and the spectral properties of the pump. Therefore, uncertainty in this virtual bandpass filter's properties are related to both pump and F_{T} characterizations. Refer to Chapter 12 for more information on parametric down conversion.

5. *Comparison of correlated photon pair and substitution calibration methods*

To verify both the detector model and measurements are valid, a comparison of the two independent primary standard methods is necessary. Such a comparison experiment was performed [19], consisting of a set of measurements where the DUT SPAD and the calibrated photodiode were alternately swapped into the setup. The experimental setup, shown in Fig. 6, allows the collection of data on the SPAD for the two calibration methods simultaneously by recording both the correlated signal (i.e. a histogram seen in Fig. 3 (b)) and the total rate of uncorrelated events, thus calibrating the SPAD with the two methods under the same conditions. After each detector swap, the alignment of the DUT active area was verified. Due to power variations of the pump laser, it was necessary to normalize the conventional calibrations. This normalization allowed the correlation-based calibration data to be compared against all the conventional runs (and not just adjacent conventional runs), because conventional data taking became insensitive to power fluctuations in the setup. To compare calibrations performed by the two independent methods, the DE of the SPAD was determined from each dataset. Because the experimental conditions were slightly different each time, the DE values η_{cond} for each SPAD trial varies within 2%. The difference in DE from run to run of the DUT is due to two reasons. First, the DUT SPAD has significant nonuniformity of response across its detection area making it difficult to exactly reproduce the DUT position between swaps. Second, because we use η_{cond}, rather than η_{DE}, its value depends on the count rate. The relative uncertainty of the detector substitution DE measurement, and the relative uncertainty of the correlated method allows for a single run comparison of the two methods to $\approx 0.25\%$.

We define the agreement between the two independent calibration methods as

$$\Delta = \frac{\overline{\eta}_{\mathrm{cond,substitution}} - \eta_{\mathrm{cond,correlated}}}{(\overline{\eta}_{\mathrm{cond,substitution}} + \eta_{\mathrm{cond,correlated}})/2}, \tag{12}$$

where $\overline{\eta}_{\mathrm{cond,substitution}}$ is the average DE over all calibrated detector runs for a fixed position of a SPAD. Ideally, if the two methods yield identical η_{cond}, $\Delta = 0$. Figure 7 shows Δ along with confidence bands at one and two standard deviations of a single comparison (0.25%) for all trials drawn against a zero-bias condition, $\Delta = 0$. We see that the differences between the two methods of calibration presented in Fig. 7 are distributed between the confidence bands, as would be expected for a normal distribution with 6 out of the 9 measurements falling within one standard deviation of zero. We combine all trials to find an average measured Δ, and its uncertainty. The mean difference between the two methods is $\overline{\Delta} = 0.14(0.14)\%$, [19]. Thus, the mean difference between the two methods is comparable to the uncertainty of comparison, supporting the equivalence of the two absolute calibration methods, and limiting any residual bias to the level of the uncertainty of the comparison.

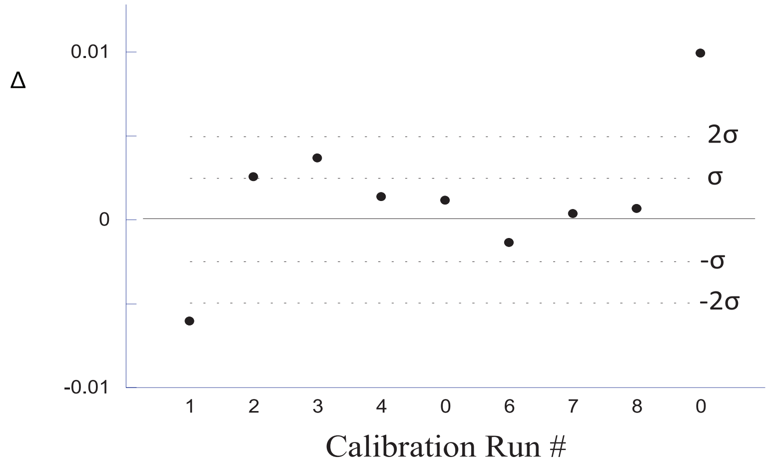

FIG. 7: Comparison between two absolute calibration methods: correlated photon pair and substitution (traceable to NIST scale). The size of the confidence bands reflects the uncertainty of each individual comparison and indicates the consistency of the overall comparison with zero bias between the two methods.

This measurement validates the detector model introduced earlier in the text to within experimental uncertainty. We expect that the detector model and the procedure for measuring its parameters would work for any non-PNR detector, regardless of its underlying physical principle of operation.

B. Transition Edge Sensors

Until this point, we have only dealt with non-photon-number-resolving detectors. In general, a photon-number-resolving detector should be characterized by its POVM [28]. The POVM formalism is introduced in Chapter 9. If a detector's efficiency does not depend on the number of incoming photons, a POVM treatment is often not necessary; such detectors can be characterized solely by their detection efficiency. We discuss here the calibration of what is referred to as full photon-number resolving capability using classification introduced in [29]. As an example, we focus on the specifics of calibrating transition edge sensor detectors (TES), c.f. Chapter 6. Calibration techniques discussed earlier may be adapted for a TES. Having full photon-number resolving capability is advantageous for radiant power measurements. On the other hand, the signal-to-noise ratio of a TES's raw analog output may make it difficult to distinguish between certain detection events, particularly when the analog signal can be attributed to detection of both n and $n+1$ photon states. The modified calibration protocols described below are designed to take advantage of new capabilities and to circumvent the shortcomings of TES technology.

1. *Radiant power calibration*

A TES detector outputs an analog signal proportional to its temperature. When a photon or photons are absorbed, the detector's temperature slightly fluctuates as it heats up and then dissipates the heat. The peak temperature change is approximately proportional to the number of photons absorbed (assuming narrow bandwidth light). A typical response waveform spans about 1 μs (see Chapter 6). A power measurement consists of collecting raw analog waveforms and extracting detection events and photon numbers for each waveform. Because a TES's temporal response is relatively slow and the raw analog signal may be noisy, calibration with a pulsed source is advantageous. In this way the precise time of detection is known, which helps with the convergence of the waveform-fitting algorithm and allows the number of detected photons to be extracted with higher accuracy. Because the detector is photon-number resolving, coherent states of light with an average number of photons per pulse $\lambda \geq 1$ can be used. In practice, this number should not exceed more than a few photons per pulse, as the accuracy with which photon number can be extracted from the response waveforms decreases significantly beyond 10 or 20 photons. In contrast, for click/no-click detectors an average number of photons per pulse should be as close to zero as practically possible. For a Poissonian input, the probability $p(k)$ of k photons arriving in any single pulse is

$$p_{\text{in}}(k) = \lambda^k e^{-\lambda}/k! \tag{13}$$

FIG. 8: Multi-attenuator setup used for a TES calibration (DUT). Reproduced from [30].

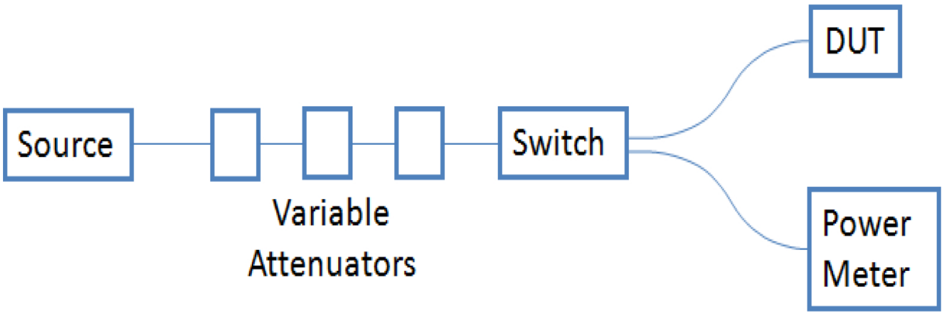

FIG. 9: Linearity calibration of a power meter with a pulsed source. Three power measurements are taken: P_1 when only shutter 1 is open; P_2 when only shutter 2 is open and P_3 when both shutters are open. For a truly linear power meter, $P_3 = P_1 + P_2$. An extra fiber mandrel is added to one of the paths to prevent interference. Reproduced from [30].

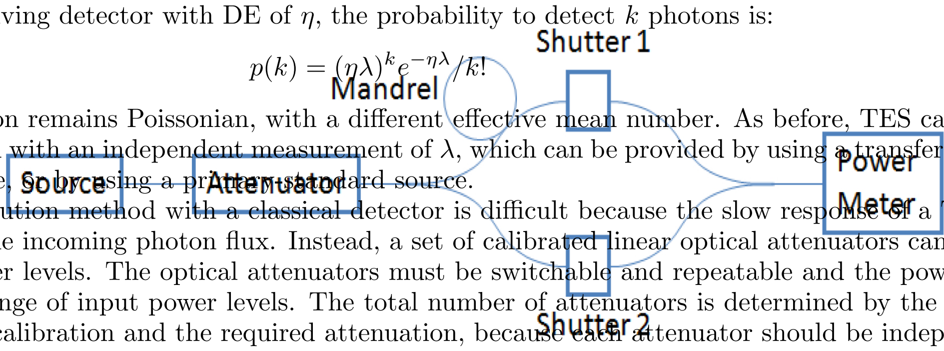

For a photon number resolving detector with DE of η, the probability to detect k photons is:

$$p(k) = (\eta\lambda)^k e^{-\eta\lambda}/k! \tag{14}$$

We see that the distribution remains Poissonian, with a different effective mean number. As before, TES calibration results should be compared with an independent measurement of λ, which can be provided by using a transfer detector and an uncalibrated source, or by using a primary-standard source.

Direct use of the substitution method with a classical detector is difficult because the slow response of a TES sets a relatively low limit on the incoming photon flux. Instead, a set of calibrated linear optical attenuators can be used to reach the required power levels. The optical attenuators must be switchable and repeatable and the power meter must be calibrated at a range of input power levels. The total number of attenuators is determined by the dynamic range of the power meter calibration and the required attenuation, because each attenuator should be independently calibrated using the power meter. When all attenuators are applied, the optical power should be suitable for a TES. The dominant uncertainty is usually a systematic error in the calibration of the power meter, combined with the uncertainties in the attenuators. A simplified diagram of a calibration setup is presented in Fig. 8. This calibration technique was implemented by Miller et al., [30]. In their setup, they used three attenuators. A similar version of a calibration setup was employed by [31], however their variable attenuator was pre-calibrated based on national standards, hence they could skip the in-situ attenuator calibration.

The optical sensor used in the measurement depicted in Fig. 8 is calibrated in two steps. First, the power meter is compared to a transfer-standard detector at the wavelength of interest in a substitution setup [32]. Secondly, the linearity of the power meter response is measured relative to the calibration power level. Consideration of the power meter's linearity is necessary for attenuator calibration. To characterize the linearity, the method of additive power measurements can be used, also known as a triplet measurement [33]. A setup for such a measurement is shown in Fig. 9. The sum of the power measured in each of the two beamsplitter arms alone is compared to the power measured when the two arms are combined. To prevent interference on the last beam splitter before the power meter, a pulsed source and an extra fiber mandrel are used. If the response is nonlinear, there will be a difference between the sum and the full-power reading of the power meter. By making many of similar measurements over the entire dynamic range of the power meter, a dynamic calibration curve is obtained.

After applying the corrections to the measured count rate for a given source flux, a high-accuracy measurement of efficiency can proceed. Reference [30] claims an excellent reproducibility of their detection efficiency measurements across a batch of samples: $\approx 2\%$ (one standard deviation), and point to fiber alignment as a major source of uncertainty.

2. Correlated calibration technique

The calibration technique based on correlated-photon pairs (see Fig. 2) can be modified for calibrating TES detectors. In [34], a SPAD detector was used as a trigger and a TES detector as a DUT. Because TES detectors are photon-number resolving, there is room for improvement of the traditional technique. Specifically, it is possible to obtain independent estimates of detection efficiency for different photon-number states, let $p_{\rm yes}(n)$ be the probability of detecting n photons by a TES when the heralding channel fires, and $p_{\rm no}(n)$ when the heralding channel does not. Then, for an ideal trigger channel, following the derivation of [34] one can write:

$$p_{\rm yes}(0) = (1-\eta)p_{\rm no}(0), \tag{15}$$

$$p_{\rm yes}(i) = (1-\eta)p_{\rm no}(i) + \eta p_{\rm no}(i-1). \tag{16}$$

where η is a detection efficiency of the entire TES channel. As before, inseparability of losses from detection efficiency presents a substantial difficulty because all the elements of the DUT optical path must be characterized separately and an overlap factor for the correlated photons with the DUT collection must also be determined. Because in many cases the TES's optical input is a single-mode fiber, this overlap is a significant factor. An accurate characterization of the overlap is challenging.

As we have shown, the trigger channel and the SPAD detector also need to be characterized to account for detections that are not related to photon pairs. Table II gives a list of important parameters in a trigger channel and their typical contribution to the overall uncertainty. The above formulae should be modified to account for false and untimely trigger events. Let ξ be the fraction of heralding events that are due to detecting a photon from a PDC pair (i.e. $(1-\xi)$ represents the number of false clicks in the heralding channel). To find ξ an additional experiment is needed, in which the parametric down-conversion process is switched on and off (for example, by controlling phase matching). This method only works if SPAD afterpulses are identified and rejected. The authors of [34] explicitly take advantage of a pulsed source to reject detections that fall outside of a short temporal window defined by the source, therefore afterpulsing is not an issue. It is thus possible to write:

$$p_{\rm yes}(0) = \xi(1-\eta)p_{\rm no}(0) + (1-\xi)p_{\rm no}(0), \tag{17}$$

$$p_{\rm yes}(i) = \xi[(1-\eta)p_{\rm no}(i) + \eta p_{\rm no}(i-1)] + (1-\xi)p_{\rm no}(i). \tag{18}$$

The above equations can be used to obtain independent values for η, based on events of different photon number. In [34], η values are found for $i = 0, 1$ and 2. These values agree to within an experimental uncertainty.

It is obviously possible to replace the SPAD in the heralding arm with another TES detector, and observe the corresponding joint photon-number distributions. A typical joint photon-number distribution obtained in this configuration is shown in Fig. 10 [35]. For each analog waveform a maximum pulse height is measured and plotted. The pulse height is proportional to total energy absorbed by a TES. Pulse heights cluster in accordance with photon number, with some dispersion due to analog noise. When the joint distribution is plotted for two detectors, a strong correlation between simultaneously detected photon numbers appears. Indeed, if for example a 4-photon state was detected by TES 1, the probability for TES 2 to detect zero photons is very low. A joint photon distribution of this kind contains information about both detection efficiency (with all channel losses included) and a more complete measurement - the POVM. While approximate values for both the detection efficiency and the POVM can be inferred from this graph, additional measurements (such as background counts) are required to reach metrological accuracy.

Note that if the overlap of correlated-photon modes is duly characterized, this calibration scheme is symmetric: in principle, either of the two detectors can be considered the trigger detector or the DUT. One can modify the setup further to take advantage of photon-number sensitivity by collecting both photons of the pair into one optical path to a single detector. Then, ideally, and in a regime of low probability of pair generation (so we can ignore multi-pair generation), we have:

$$p(2) = \eta^2 q(2), \tag{19}$$

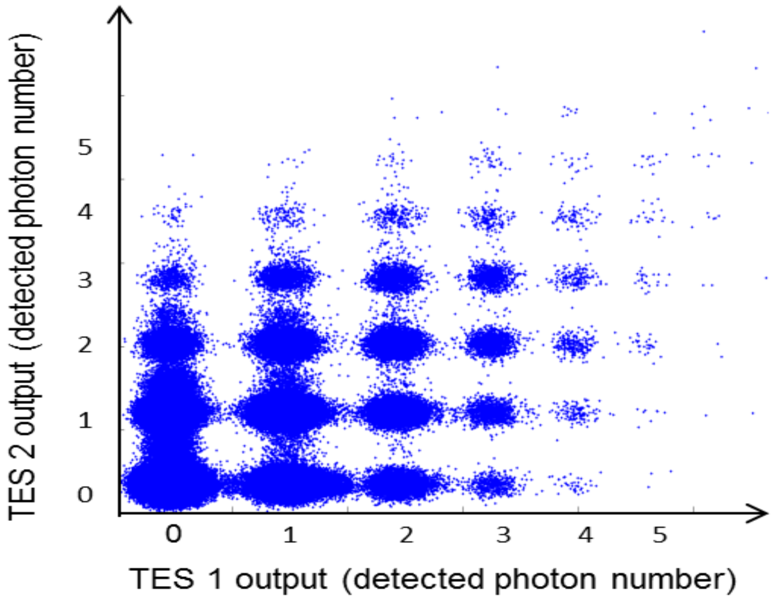

FIG. 10: An output of a PDC source measured with two TES detectors (based on the pulse heights of the TES output waveforms). Photon number is assigned to each cluster peak. Strong photon-number correlation is evident: when a high-photon-number state is detected in one arm, the probability of detecting no photons in the other arm is lower than that of detecting one, two or more. Image courtesy of Thomas Gerrits [35].

$$p(1) = 2\eta(1-\eta)q(2), \tag{20}$$

$$p(0) = (1-\eta)q(2) + q(0). \tag{21}$$

Here $p(n)$ are probabilities to detect n-photons in a trial. $q(n)$ are probabilities to generate an n-photon state, and η includes all coupling losses and detection efficiency for each of the two photons in the pair. These losses are assumed to be symmetric, but they may be asymmetric, because of the mode overlap. Because photons are generated in pairs, $q(1) = 0$. This leaves us with a set of 3 equations with 3 unknowns.

We have explored a few variants of a correlated technique suitable for TES detectors. We note that other variants exist, such as one that uses the DUT as its own trigger [36, 37]. The above results are directly applicable to other detectors with full PNR capability.

V. CONCLUSION

We have presented the most common methods for calibrating single-photon detectors. We covered both radiant-power-based and correlated-photon-based calibration techniques, showcasing SPAD and TES calibration. It is evident that to achieve true metrological accuracy these seemingly simple methods require careful consideration and attention. Even a basic measurement of radiant power with such detectors requires additional knowledge of both source (spectrum, statistics), and detector (photon-number-resolving capabilities, recovery time, afterpulsing, etc.), as well as an appropriate detector model. SPAD calibration procedures can be adapted for most non-PNR detectors. Similarly, TES calibration procedures can be adapted to other detectors with full-PNR capability. Other photon-number-resolving detectors, and most notably, multiplexed arrangements of non-number resolving detectors (c.f. Chapter 7), cannot be properly calibrated with these methods without substantial modifications. A better approach is to apply a POVM formalism, as described in the next chapter.

---

[1] M. Planck, Verhandlungen der Deutschen Physikalischen Gesellschaft **2**, 237 (1900).
[2] W. H. Louisell, A. Yariv, and A. E. Siegman, Physical Review **124**, 1646 (1961).
[3] B. Y. Zeldovich and D. N. Klyshko, Sov. Phys. JETP Lett. **9**, 40 (1969).
[4] F. Zernike and J. E. Midwinter, *Applied Nonlinear Optics* (New York: Wiley, 1973).
[5] D. C. Burnham and D. L. Weinberg, Physical Review Letters **25**, 84 (1970).
[6] D. N. Klyshko, Sov. J. Quantum Electron. **7**, 591 (1977).
[7] D. N. Klyshko, Sov. J. Quantum Electron. **10**, 1112 (1981).
[8] A. A. Malygin, A. N. Penin, and A. V. Sergienko, Sov. J. Quantum Electron **11**, 939 (1981).
[9] S. R. Bowman, Y. H. Shih, and C. O. Alley, in *Laser Radar Technology and Applications I*, edited by J. M. Cruickshank and R. C. Harney (SPIE, 1986), vol. 663 of *Proc. SPIE*, pp. 24–29.
[10] K. D. Rarity, J. G.and Ridley and P. R. Tapster, Appl. Opt. **26**, 4616 (1987).
[11] A. N. Penin and A. V. Sergienko, Appl. Opt. **30**, 3582 (1991).
[12] V. M. Ginzburg, N. Keratishvili, E. L. Korzhenevich, G. V. Lunev, A. N. Penin, and V. Sapritsky, Opt. Eng. **32**, 2911 (1993).
[13] P. G. Kwiat, A. M. Steinberg, R. Y. Chiao, P. H. Eberhard, and M. D. Petroff, Appl. Opt. **33**, 1844 (1994).
[14] A. Migdall, R. Datla, A. Sergienko, J. S. Orszak, and Y. H. Shih, Metrologia **32**, 479 (1995).
[15] G. Brida, S. Castelletto, I. P. Degiovanni, C. Novero, and M. L. Rastello, Metrologia **37**, 625 (2000).
[16] G. Brida, S. Castelletto, I. P. Degiovanni, M. Genovese, C. Novero, and M. L. Rastello, Metrologia **37**, 629 (2000).
[17] A. Ghazi-Bellouati, A. Razet, J. Bastie, M. Himbert, I. Degiovanni, S. Castelletto, and M. Rastello, Metrologia **42**, 271 (2005).
[18] X.-H. Chen, Y.-H. Zhai, D. Zhang, and L.-A. Wu, Opt. Lett. **31**, 2441 (2006).
[19] S. V. Polyakov and A. L. Migdall, Optics Express **15**, 1390 (2007).
[20] T. J. Quinn, Metrologia **34**, 61 (1997).
[21] M. Ware and A. L. Migdall, Journal of Modern Optics **15**, 1549 (2004).
[22] A. L. Migdall, IEEE Transactions on Instrumentation and Measurement **50**, 478 (2001).
[23] M. Ware, A. Migdall, J. C. Bienfang, and S. V. Polyakov, Journal of Modern Optics **54**, 361 (2007).
[24] A. Spinelli, L. M. Davis, and H. Dautet, Rev. Sci. Instrum. **67**, 55 (1996).
[25] W. Schmunk, M. Rodenberger, S. Peters, H. Hofer, and S. Kuck, Journal of Modern Optics **58**, 1252 (2011).
[26] T. C. Larason, S. S. Bruce, and A. C. Parr, Tech. Rep., NIST Special Publication 250-41 (1997).
[27] S. W. Brown, G. P. Eppeldauer, and K. R. Lykke, Appl. Opt. **45**, 8218 (2006).
[28] J. S. Lundeen, A. Feito, H. Coldenstrodt-Ronge, K. L. Pregnell, C. Silberhorn, T. C. Ralph, J. Eisert, M. B. Plenio, and I. A. Walmsley, Nature Physics **5**, 27 (2009).
[29] M. D. Eisaman, J. Fan, A. Migdall, and S. V. Polyakov, Appl. Opt. **82**, 071101 (2011).
[30] A. J. Miller, A. E. Lita, B. Calkins, I. Vayshenker, S. M. Gruber, and S. W. Nam, Optics Express **19**, 9102 (2011).
[31] D. Fukuda, G. Fujii, T. Numata, K. Amemiya, A. Yoshizawa, H. Tsuchida, H. Fujino, H. Ishii, T. Itatani, S. Inoue, et al., Optics Express **19**, 870 (2011).
[32] J. H. Lehman and X. Li, Appl. Opt. **38**, 7164 (1999).
[33] I. Vayshenker, S. Yang, X. Li, T. R. Scott, and C. C. L., NIST Special Publication **25056** (2000).
[34] A. Avella, G. Brida, I. P. Degiovanni, M. Genovese, M. Gramegna, L. Lolli, E. Monticone, C. Portesi, M. Rajteri, M. L. Rastello, et al., Optics Express **19**, 23249 (2011).
[35] T. Gerrits (2011), private communication.
[36] A. Czitrovszky, A. Sergienko, P. Jani, and A. Nagy (1999), vol. 3749 of *Proc. SPIE*, p. 422.
[37] A. Czitrovszky, A. Sergienko, P. Jani, and A. Nagy, Laser Physics **10**, 86 (2000).